Corrosion Science 133 (2018) 132–140

Contents lists available at ScienceDirect

Corrosion Science

journal homepage: www.elsevier.com/locate/corsci

On the severe localized corrosion susceptibility of the AA2198-T851 alloy

João Victor de Sousa Araujo[a,*], Uyime Donatus[a], Fernanda Martins Queiroz[b], Maysa Terada[c], Mariana Xavier Milagre[a], Maicon Cavalieri de Alencar[a], Isolda Costa[a]

[a] Instituto de Pesquisas Energéticas e Nucleares,IPEN/CNEN, Av. Prof. Lineu Prestes, 2242, São Paulo, Brazil
[b] Escola Politécnica da Universidade de São Paulo, EPUSP, Av. Prof. Mello Moraes, 2463, São Paulo, Brazil
[c] Brazilian Nanotechnollogy National Laboratory, LNNano/CNPEN, Rua Giuseppe Máximo Scolfaro, 10.000 Polo II de Alta Tecnologia de Campinas, Campinas, Brazil

ARTICLE INFO

Keywords:
A. Aluminum
B. TEM
B. SEM
C. Pitting corrosion

ABSTRACT

The time dependent susceptibility of AA2198-T851 Al-Cu-Li alloy to severe localized corrosion in 0.01 mol L^{-1} NaCl solution has been investigated by immersion and SVET tests. The results reveal that the propagation of severe localized corrosion, in the alloy, is crystallographic and it is associated with the slip bands in the individual grains of the alloy. The slip bands caused uneven precipitation of the active T1 particles. Also, oscillations in SVET current density values associated with deposition and detachment of corrosion products were observed. Furthermore, the intensity of corrosion activities increased over time for open or partially covered pits.

1. Introduction

The interest in the potential properties of Al-Li alloys started in the 50's when the first generation Al-Li alloys were used in specialized applications. However, they were not found proper for aero-structural parts due to their low short-transverse fracture toughness, poor corrosion resistance, and poor thermal stability [1,2]. Efforts were made to overcome these challenges in the second generation Al-Li alloys by changing the alloy composition and thermomechanical processing routes, but the second generation Al-Li alloys were still associated with high anisotropy of tensile properties [3].

The third generation Al-Li alloys (with lower Li contents compared with the previous generations) were mainly developed for military and space applications. The aim of developing the third generation Al-Li alloys was to meet the demands of future commercial airframes [4]. This generation, apparently, has overcome the main drawback of mechanical anisotropy, and it is gaining increasing interest and growing usage in aerospace applications due to their remarkable lightweight. The alloys are currently being used in modern aircrafts [5–7]. According to literature, the third generation Al-Li alloys show improved mechanical properties relative to the conventional 2xxx and 7xxx series [3,8].

Despite the improvements in mechanical properties, the third generation of Al-Li alloys are still susceptible to localized forms of corrosion which is associated with the high reactivity of Li and the resultant Li-containing intermetallic phases [9]. The localized corrosion resistance of these types of alloys has been of great concern, and much research work has been carried out on the alloys of the third generation [10–18].

The corrosion properties and performance of Al-Li alloys are dependent on alloy composition and microstructural features. Addition of Cu and Li into the aluminum alloy leads to precipitation of phases such as T1 (Al_2CuLi) and δ' (Al_3Li). The T1 phase is the main strengthening phase in these alloys but it has also been strongly associated with the severe localized corrosion of the Al-Li alloys [10–18].

Two types of corrosion attack associated with T1 phase has been reported in literature: (i) dissolution of this phase near a precipitation free zone resulting in the formation of small cavities; and (ii) selective dissolution of the T1 phase along with the dissolution of the adjacent aluminum matrix, leaving large pits [13]. It has also been proposed that the T1 phase might either undergo selective dissolution along with the dissolution of the adjacent Al matrix forming large pits [15], or dissolve near to the precipitate free zone forming small cavities [16].

Ma et al. [17] studied the corrosion behavior of the AA2099-T83 alloy in 3.5 wt.% NaCl solution and observed two types of localized corrosion. The first type was identified as a type of attack associated with the constituent particles containing aluminum, copper, iron and manganese. This type of attack was also related to the distribution of the constituent particles in the alloy. As these types of particles were cathodic to the matrix, the attack occurred at the matrix surrounding them. The second type of localized corrosion was called severe localized corrosion and it was characterized by hydrogen gas evolution and corrosion rings around the attacked areas [18]. This type of localized corrosion has also been previously reported in literature for the

* Corresponding author.
E-mail address: joao-neutron@hotmail.com (J.V. de Sousa Araujo).

https://doi.org/10.1016/j.corsci.2018.01.028
Received 14 November 2017; Received in revised form 28 December 2017; Accepted 20 January 2018

AA2024-T3 [19–23].

According to Ma et al. [17], the origin of severe localized corrosion in the AA2099-T83 alloy is related to selective dissolution of the T1 phase. This phase precipitates preferentially at grain/subgrain boundaries and dislocations within grains and preferential attack occurs at grains that were exposed to great plastic deformation when subjected to cold stretching prior to aging and, consequently, presented increased density of T1 phase after aging. Due to the high electrochemical activity of the T1 phase, corrosion attack occurred preferentially in the more deformed grains.

Pitting corrosion resistance of Al-Li alloys, including the AA2198 alloy, has been reported in literature [24–26]. Alexopoulos et al. [27] studied the mechanical properties degradation of the AA2198 alloy due to corrosion exposure. According to the authors, this alloy is more resistant to corrosion than the AA2024 alloy in EXCO solution. Moreto et al. [26] studied the localized corrosion behavior of the AA2198-T851 and compared the results with that of the AA2524-T3 in naturally aerated 0.6 mol L^{-1} NaCl solution by localized electrochemical techniques. The authors concluded that the AA2198-T851 presented higher pitting resistance when compared with the AA2524-T3 and suggested that the first alloy could be a potential replacement for the conventional AA2524-T3 alloy. However, in another work, Moreto et al. [28] showed that the 2198 alloy is more susceptible to corrosion compared with conventional alloys, such as 2524 and 7050, based on corrosion potential and pitting potential values. These clearly show that already reported results on the localized corrosion resistance of the AA2198 alloy are controversial. To buttress this point, previous results obtained in our laboratory [29] that compared the localized corrosion resistance of the alloys AA2198-T851, AA2524-T3 and AA2024-T3, showed that the first alloy presented the highest susceptibility to localized corrosion among the studied ones. Also, in a very recent report by Donatus and co-workers [30] it was revealed that the AA2198-T851 alloy is more susceptible to corrosion compared with the AA2024-T3 alloy. However, the corrosion mechanisms in the two alloys are different. While the predominant corrosion mechanism in the AA2198-T851 is intragranular, that in the AA2024-T3 is intergranular.

Thus, based on the conflicting results in literature and the fact that works on the corrosion mechanism of the AA2198-T851 alloy are still very rare, there is need for further research in order to advance the understanding of localized corrosion behavior of the AA2198-T851 alloy. Therefore, the aim of this study is to investigate the localized corrosion resistance of this alloy by means of monitoring the corrosion development on the alloy during immersion tests using a combination of scanning vibrating electrode technique and microscopic observation after various periods of exposure to 0.01 mol L^{-1} sodium chloride solution.

2. Experimental

The chemical composition obtained from Inductively Coupled Plasma Optical Emission Spectrometry (ICP-OES) and the nominal composition of the AA2198-T851 alloy used in this study are presented in Table 1.

2.1. Sample preparation and microscopy

The surfaces of the samples were successively ground and polished to 1 µm surface finish using silicon carbide papers (of #800, #1200 and #4000 grit sizes) and diamond pastes (3 µm and 1 µm). Following mechanical polishing, the samples were degreased in acetone (analytical grade), rinsed in deionized water and dried under a cool air stream. After polishing, samples used for the revelation of grain sizes and grain features were etched using a solution comprising 2% HF and 25% HNO_3. These samples were only used for this purpose and were not used for other experiments.

For transmission electron microscopy (TEM), 3.0 mm discs were punched from mechanically polished samples, followed by twin-jet electropolishing at 20 V in a solution comprising 30% nitric acid and 70% methanol. The solution was kept in the range of −35 °C.

Also, for the removal of corrosion products after corrosion tests, 30% HNO_3 solution was employed and the treatment lasted 60 s for each sample.

Optical microscopy (OM) and scanning electron microscopy (SEM) images of the AA2198-T851 surface were acquired using a Leica DMLM coupled optical microscope and a Quanta 650 field emission gun—scanning electron microscope (FEG-SEM). A JEM-2100F Transmission Electron Microscope (TEM) operating at 200 kV was employed for TEM analyses.

Table 1
Chemical composition (wt.%) of the AA2198-T851 alloy obtained by ICP-OES.

Analyzed		Nominal composition	
Elements	wt.%	Elements	wt.%
Cu	3.31	Cu	(2.9–3.5)
Mg	0.31	Mg	(0.25–0.8)
Mn	–	Mn	(0.1–0.5)
Li	0.96	Li	(0.8–1.1)
Si	0.03	Si	(0.08 máx)
Fe	0.03	Fe	(0.3 máx)
Ti	0.03	Ti	(0.1 máx)
Zr	0.40	Zr	(0.04–0.18)
Ag	0.25	Ag	(0.1–0.5)
Zn	0.006	Zn	(0.35 máx)
Al	Balance	Al	Balance

2.2. Immersion test

Immersion test was performed by exposing samples to naturally aerated 0.01 mol L^{-1} NaCl solution at (22 ± 1) °C. The samples were removed from solution after different periods of exposure (1 h, 2 h, 4 h, 8 h, 12 h, 24 h), rinsed in deionized water and dried in a hot air stream. Subsequently, the exposed surfaces were analyzed under the optical and scanning electron microscopes.

2.3. Scanning vibrating electrode technique

Scanning vibrating electrode technique (SVET) tests were carried out using an Applicable Electronics™ SVET machine that is controlled by Automated Scanning Electrode Technique (ASET 4.0) software. Insulated Pt–Ir probe was used as the vibrating electrode for the SVET system. A 15 µm diameter platinum sphere was electrodeposited at the tip of the probes prior to the start of SVET tests.

In addition, prior to the SVET tests, the machine was calibrated using a current source connected to a calibration electrode at a distance of 150 µm. A current value of 60 nA was used for the calibration. The conductivity of the solution to be used was inputted into the ASET 4 software. With the inputted conductivity, the potential difference values recorded by the SVET were automatically converted to current density values.

For the SVET test, the probe (vibrating in planes perpendicular (Z) and parallel (X) to the sample's surface) was placed at (100 ± 3) µm above the surface. The amplitude of vibration was 19 µm, and the vibrating frequencies of the probe were 174 Hz (X) and 73 Hz (Z). 35 × 25 points were obtained for each SVET map. The time lag between the each current density data-point acquired was 0.5 s, and the scan step interval was 200 µm. All experiments were performed in a Faraday cage at (20 ± 2) °C. The AA2198-T851 alloy sample used as working electrode was embedded in epoxy resin. The surface of the alloy was successively polished to a 1 µm surface finish. An adhesive tape and the epoxy resin were used as a reservoir for the electrolyte. Experiments were performed in 0.005 mol L^{-1} NaCl for 24 h, and SVET

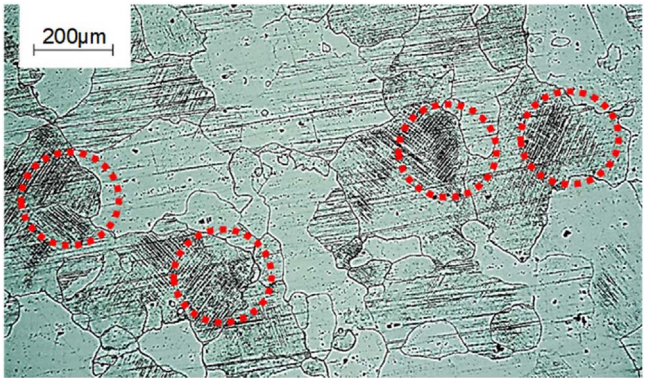

Fig. 1. Optical micrograph of the AA2198-T851 alloy used in this investigation.

maps were obtained every 1 h. In situ images of the corroding AA2198-T851 surface were obtained at timed intervals during the SVET measurements.

3. Results and discussion

3.1. Microstructural characterization

An optical micrograph showing the microstructure of the AA2198-T851 alloy is presented in Fig. 1. Slip bands in single grains are highlighted by red circles. Slip bands are due to the development of inhomogeneous plastic strains in high stacking fault energy materials in which cross-slip is eased [31]. They are characterized by the presence of dislocation accumulation in bands separated by relatively dislocation-free regions [32]. Slip bands in aluminum alloys have been reported in literature [32–34]. In this alloy, the slip bands play a significant role in the propagation of severe localized corrosion or corrosion pathways within the individual grains of the alloy, as will be revealed in section 3.2 below.

Fig. 2 shows transmission electron microscopy (TEM) micrographs of the AA2198-T851 alloy. The micrographs reveal that the predominant phase in the alloy is the T1 phase. This was confirmed by the analysis of the selected area diffraction (SAED) pattern presented in Fig. 2(c). T1 precipitate has a hexagonal crystal structure and appears as thin needles. As revealed in the micrographs, the T1 particles appear to be homogeneously distributed inside the grains. However, the T1 phase is preferentially precipitated at dislocations [35–38], subgrain and/or grain boundaries [39]. Thus, in the slip bands revealed in Fig. 1, the T1 particles preferentially precipitates at the banded regions with higher dislocation density. The TEM micrographs also reveal the presence of composite Al_3Zr/Al_3Li (β'/δ') precipitate in the alloy. This precipitate has no direct effect on the corrosion resistance of this alloy. However, its presence can cause surface oxide discontinuities, which in turn can affect the corrosion resistance of the alloy.

3.2. Corrosion tests

Optical micrographs showing the surface of the AA2198-T851 alloy at increasing periods of immersion in the 0.01 mol L^{-1} NaCl solution are displayed in Fig. 3. After 1 h of immersion test, small cavities

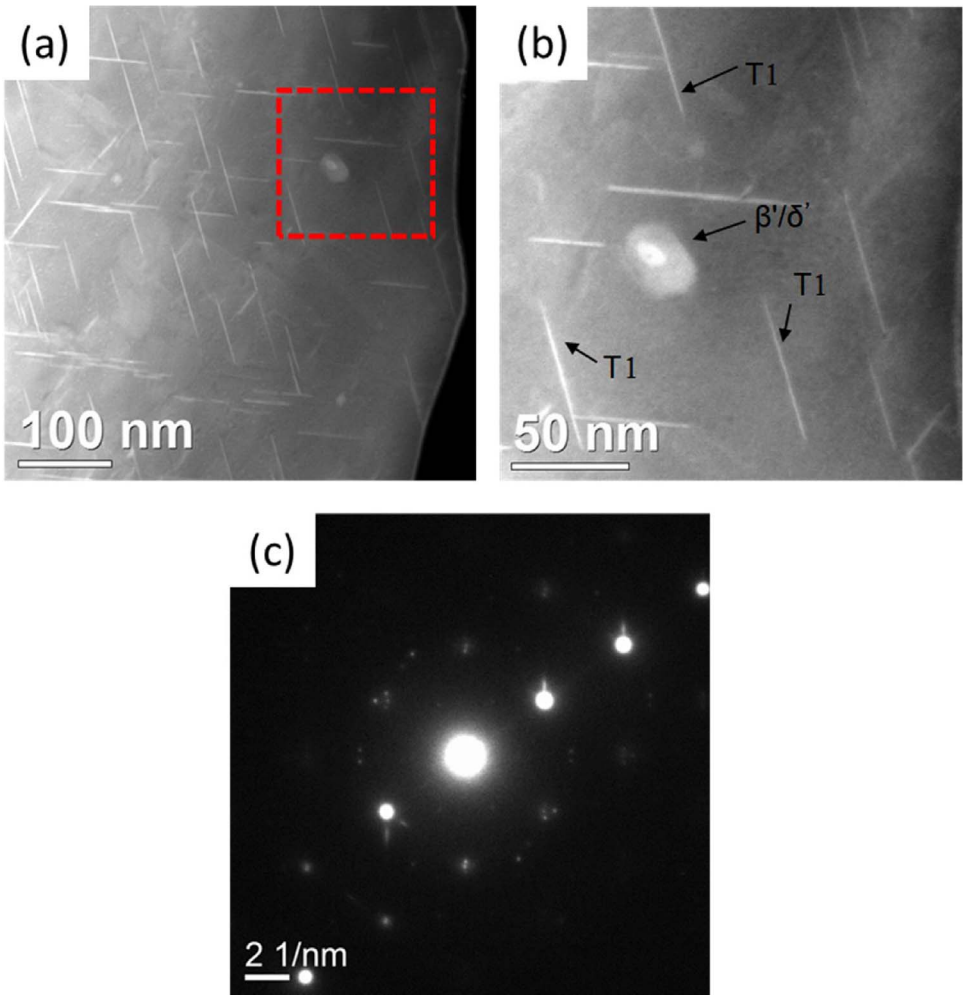

Fig. 2. (a) TEM images of the AA2198-T851 alloy showing the T1 phase and Al_3Zr/Al_3Li composite phase. (b) TEM image of the area marked in (a) at higher magnification. (c) SAED pattern image near Al [101] zone axis.

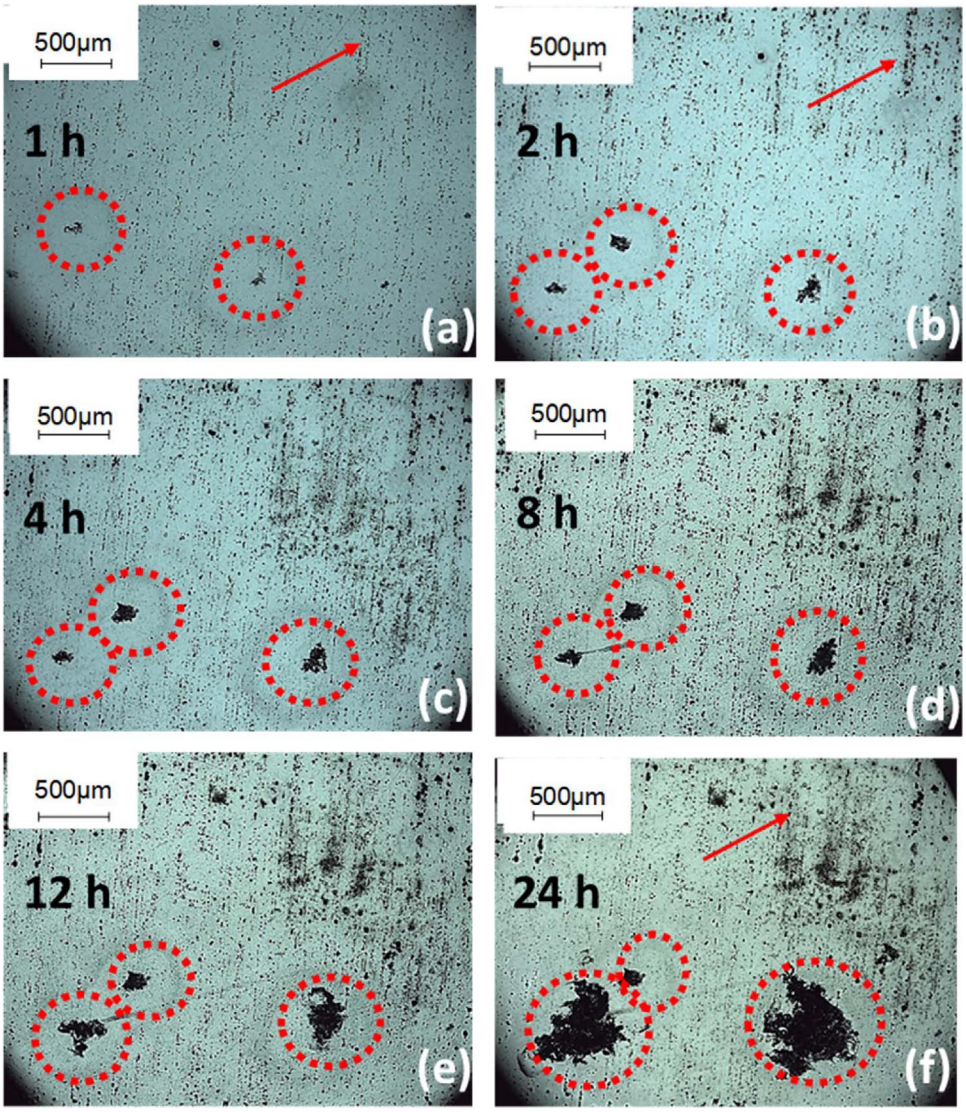

Fig. 3. Optical micrographs of the AA2198-T851 alloy exposed to NaCl 0.01 mol L^{-1} solution for (a) 1 h; (b) 2 h; (c) 4 h; (d) 8 h; (e) 12 h; (f) 24 h respectively.

associated with the activities of constituent particles were seen all over the exposed surface. After exposure to the electrolyte, some of the areas surrounding this type of particles were rapidly activated (as indicated by the red arrows), whereas other areas only became electrochemically activated after a while. This can be clearly seen by comparing the micrographs obtained after 1 h, 2 h, 4 h and 8 h respectively. For periods longer than 8 h, the attacked areas associated with the constituent particles did not increase significantly. The formation of trenches and/or small cavities due to the activities of the constituent particles is clearly revealed in Fig. 4. The micrographs display the surface of an AA2198-T851 alloy sample exposed to the 0.01 mol L^{-1} NaCl solution for 24 h and, evidently, show that the matrix (which is preferentially attacked) is anodic to the constituent particles. These particles were characterized by FEG-SEM and were composed of Al, Fe and Cu (as evident from the EDX profile in Fig. 4(c)) with Cu contents in the range of 27–30 wt%.

Another important feature observed after 1 h of immersion test was the evolution of a different type of corrosion (that was not associated with the activities of the constituent particles). This was evident by the appearance of attacked spots surrounded by circular areas (corrosion rings) with little or no trace of attack. Presented in Fig. 5 is an optical micrograph clearly showing the attacked site and protected region within a corrosion ring. Thus, the areas within the corrosion rings are cathodically protected by the anodic reactions occurring at the center of the pits. These corrosion features are typical of severe localized corrosion sites associated with regions where hydrogen bubbles are observed during immersion tests, as already described in literature for the AA2099 alloy [16–18]. After initiation, the attacked areas, associated with this type of corrosion, increased with time, and the increments were especially pronounced between 8 h and 24 h, Fig. 3(a)–(f).

Precipitation of corrosion products was also seen on some of the severe localized corrosion sites (Fig. 6), mainly outside the pits and this was due to pH increase at cathodic sites. The effect of the deposition of corrosion products are later discussed in the analyses of the SVET results. On the severe localized corrosion sites, crystallographic type of attack was observed, indicating that the propagation of the severe localized corrosion occurs crystallographically. The crystallographic attack was more evident at longer immersion periods, Fig. 7. This propagation mode is associated with the slip bands revealed in Fig. 1. As mentioned earlier, the slip bands are characterized with dislocation-dense and dislocation-free regions in alternate manner. Given that the T1 phase precipitates preferentially at sites with higher dislocation density, this implies that the individual grains of the alloy are composed of T1-rich and T1-free bands in an alternate manner. This argument is in agreement with the recent works of Donatus et al. [30] and Zhang et al. [40] that revealed active bands with higher volume fraction of T1 phase. These bands are alternately aligned with more noble bands comprising lower volume fraction of the T1 phase in the grains of

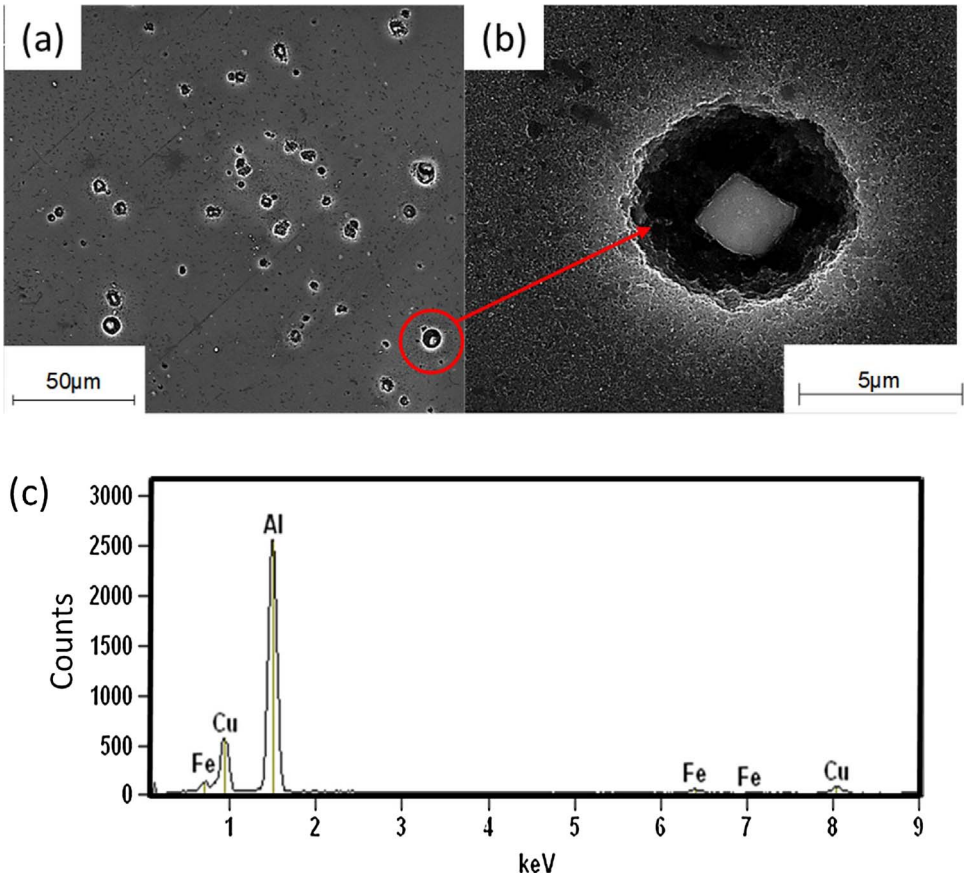

Fig. 4. (a)-(b)SEM micrographs of 2198-T851 alloy after 24 h in 0.01 mol L^{-1} NaCl solution. (c) Typical EDX profile of the cathodic constituent particle.

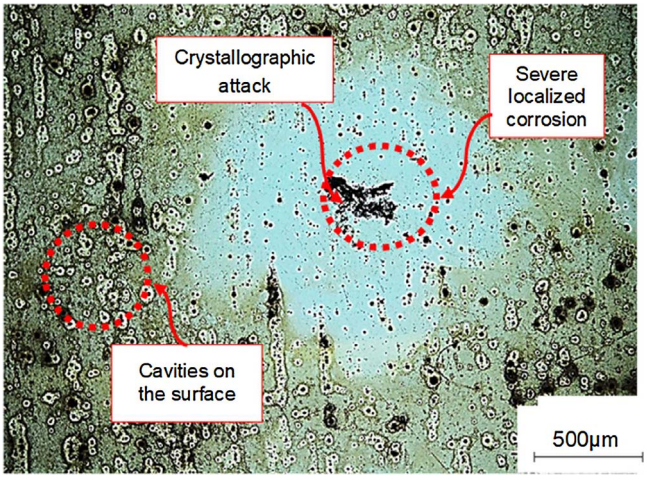

Fig. 5. Optical micrograph showing the surface of the AA2198-T851 alloy after 24 h of immersion in 0.01 mol L^{-1} NaCl solution.

AA2198-T851 alloy. Zhang and co-workers [40] also clearly showed alternate bands of higher volume fraction and lower volume fraction of T1 particles in the grains of a different new generation Al-Cu-Li alloy. In addition, these bands have been shown to be parallel to $\{111\}_{Al}$ indicating that the corrosion propagation in this alloy is grain orientation dependent.

Furthermore, anisotropy of localized corrosion kinetics in aluminum alloys has also been reported by Zhang and Frankel [41,42] and Ma et al. [15–19]. According to these last authors, plastic deformation is highly dependent on grain orientation. Consequently, the more deformed grains are more reactive and are more susceptible to localized corrosion. Guèrin et al. [43] also reported that grains in (111) orientation are more susceptible to corrosion. Ma et al. [15–19] suggested that the grains with high density of crystallographic defects (dislocations) are thermodynamically more active. This was explained by the fact that during artificial aging they act as preferential sites for nucleation and growth of T1 phase (Al_2CuLi). These grains were reported to be highly susceptible to localized corrosion, due to their high T1 phase concentration which is more electrochemically active than the aluminum matrix [44]. This is also in agreement with the optical micrographs in Fig. 1 which showed that some grains in the AA2198-T851 alloy present higher deformation (grains surrounded by red circles) and higher concentrations of T1 phase. Nonetheless, the preferential precipitation of T1 particles at dislocations is the main reason for the observed severe intragranular corrosion propagating crystallographically.

A corrosion mechanism has been proposed for the severe localized corrosion in Al-Cu-Li alloys [45]. As mentioned earlier, this type of attack is attributed to the activities of T1 particles. The initially anodic T1 phase, with respect to the matrix, undergoes selective leaching of its Li and Al components. Subsequently, this leads to a Cu-rich remnant, which consequently makes the particle cathodic with respect to the matrix. Following this, anodic dissolution of the surrounding matrix begins. Since T1 phase tends to precipitate preferentially at dislocations, the highly deformed grains are the sites most prone to severe localized corrosion. Corrosion propagates by crystallographic attack at grains orientated in directions associated with high deformation and penetrates deep in the alloy. The high electrochemical activity results in the deposition of large amounts of corrosion products at the mouths of the pits. Generally, the deposition of corrosion products leads to differential aeration between the inner parts of the pits and the outer surface. Besides, at the corrosion front, hydrolyses of cations lead to high concentration of hydrogen ions (pH decrease), and together with chloride ingress (for electro-neutrality), the anolyte solution at the corrosion front is very aggressive and this makes the process autocatalytic. However, what was observed in this work is that the attack on

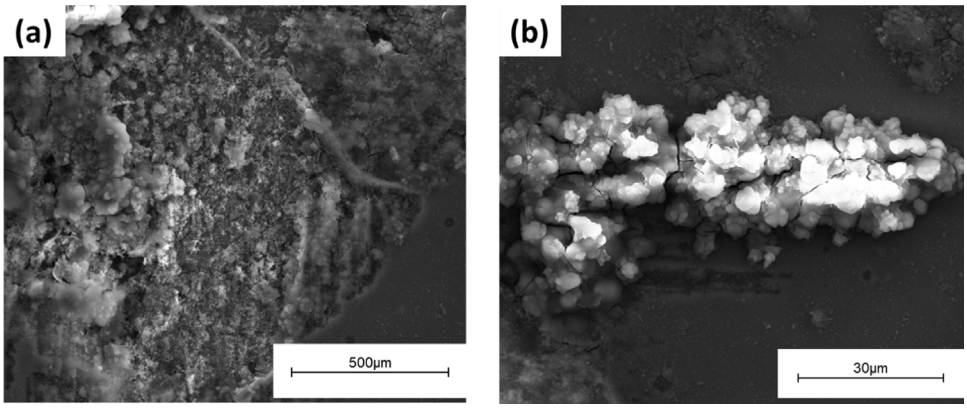

Fig. 6. SEM micrographs of the AA2198-T851 alloy after 13 h in 0.01 mol L^{-1} NaCl.

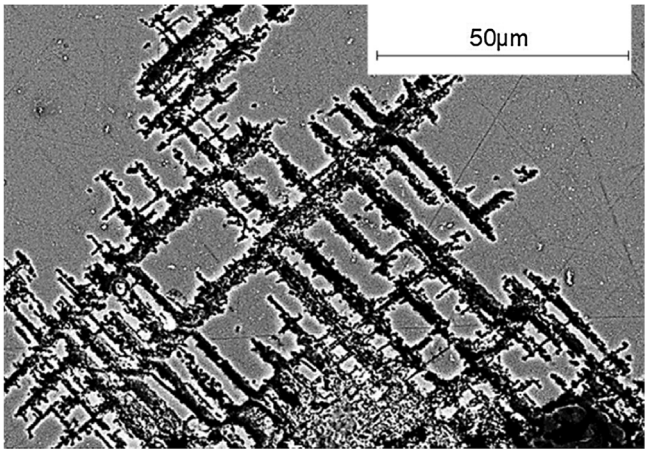

Fig. 7. SEM micrographs of the 2198-T851 alloy after 24 h in 0.01 mol L^{-1} NaCl.

open pits tends to be more intense compared with covered pits. This is apparent in Fig. 3 where the open pits kept widening with exposure time. Because of the interruptions, as the samples were removed from the solution at timed intervals, rinsed, air dried and examined, corrosion products were constantly detached from the pits mouth. Thus, on re-immersion, the mouths of the pits or the severely corroded areas were uncovered with corrosion products. This leads to exposure of unpassivated surface areas in the severe localized corrosion sites.

The development of localized attack was also monitored by SVET maps. The maps were obtained at each hour of exposure to 0.05 mol L^{-1} NaCl solution for 24 h. The maps obtained at 1 h, 2 h, 4 h, 8 h, 12 h and 24 h of exposure are shown in Fig. 8. In the SVET maps, red represents peak anodic activities while blue represents peak cathodic activities, as indicated in the current density scale bar in Fig. 8.

SVET maps allowed monitoring of the evolution of the corrosion sites with time of immersion. It is important to mention that given the high current density values associated with the sites of severe localized corrosion, the comparatively lower current density values associated with the activities of the constituent particles were not detected in the maps. Fig. 8 shows that severe localized corrosion sites (indicated by the numbers 1–7 on the maps) were initiated from the first hour of immersion. For some severe localized corrosion sites, the anodic current density values became insignificant with time of immersion; and from 14 h onwards, only one area (indicated by 4) was apparently active at the surface of the alloy. However, the reduced activities at the sites of severe localized corrosion during the early hours of immersion were due to deposition of corrosion products at the mouths of the pits.

Examination of in situ images obtained during the SVET measurements show that activation caused by the activities of constituent particles occurs at the initial periods of immersion. However, between 4 h and 6 h, accumulation of corrosion product became evident at some sites. After 8 h, corrosion rings became apparent. Although corrosion products accumulated at the site indicated as 4, the pit mouth was not covered by the products and the site remained active until the test was terminated after 24 h.

Current density peak values obtained by SVET at the center of sites 4, 5, 6 and 7 were plotted as a function of time and the results are shown in Fig. 9. The curves show decrease in current density values, attributed to deposition of corrosion products, at the early hours of exposure to the electrolyte for sites 4, 5 and 6; but for site 7, current density values only started to decrease after about 10 h. However, the current densities associated with site 4 oscillated during the period of test due to deposition and detachment of corrosion products from the surface; but after 16 h of test, it increased continuously until the test was terminated. Micrographs obtained prior to removal of corrosion products show that site 4 was only partially covered with corrosion products, as presented in Fig. 10. Thus, for a partially covered or uncovered pit mouth (site 4, as an example), the corrosion activity increases over time. This explains why the pits initiated at the early hours of the constantly interrupted immersion test (Fig. 3) kept increasing in size with time. In contrast, for a covered pit (sites 5, 6 and 7, as examples), the corrosion activity reduces over time. Thus, the SVET results reveal that corrosion products play a key role in the overall extent of corrosion.

The sample surface tested by SVET was examined after removal of corrosion products and it is shown in Fig. 11. The magnified micrographs from the different severe localized corrosion sites (Fig. 11(c)–(h)) clearly show that site 4 was the most corroded one and this is because it was only partially covered with corrosion products at later hours of the exposure test (as earlier mentioned). Corrosion products were observed on the pit in site 5 (Fig. 11(g)), even after treatment for removal of corrosion products. This also explains why the anodic current density values in site 5 became insignificant over time. Again, crystallographic type of propagation was observed in the severe localized corrosion sites. However, the crystallographic propagation mode appeared to be slightly different from zone to zone. This is because the attacks at the different zones occurred in grains oriented differently. As mentioned earlier, this observation is associated with the preferential precipitation of T1 phase at orientation dependent slip band regions with higher dislocation density. Consequently, severe localized corrosion initiation and propagation modes will be dependent on grains orientations with respect to the exposed surface.

4. Conclusions

The AA2198-T851 investigated in this study showed high susceptibility to severe localized corrosion which was observed from the first hours of exposure to 0.01 mol L^{-1} NaCl solution. The severe localized corrosion was intragranular but the propagation pathway was crystallographic. The crystallographic propagation was associated with the

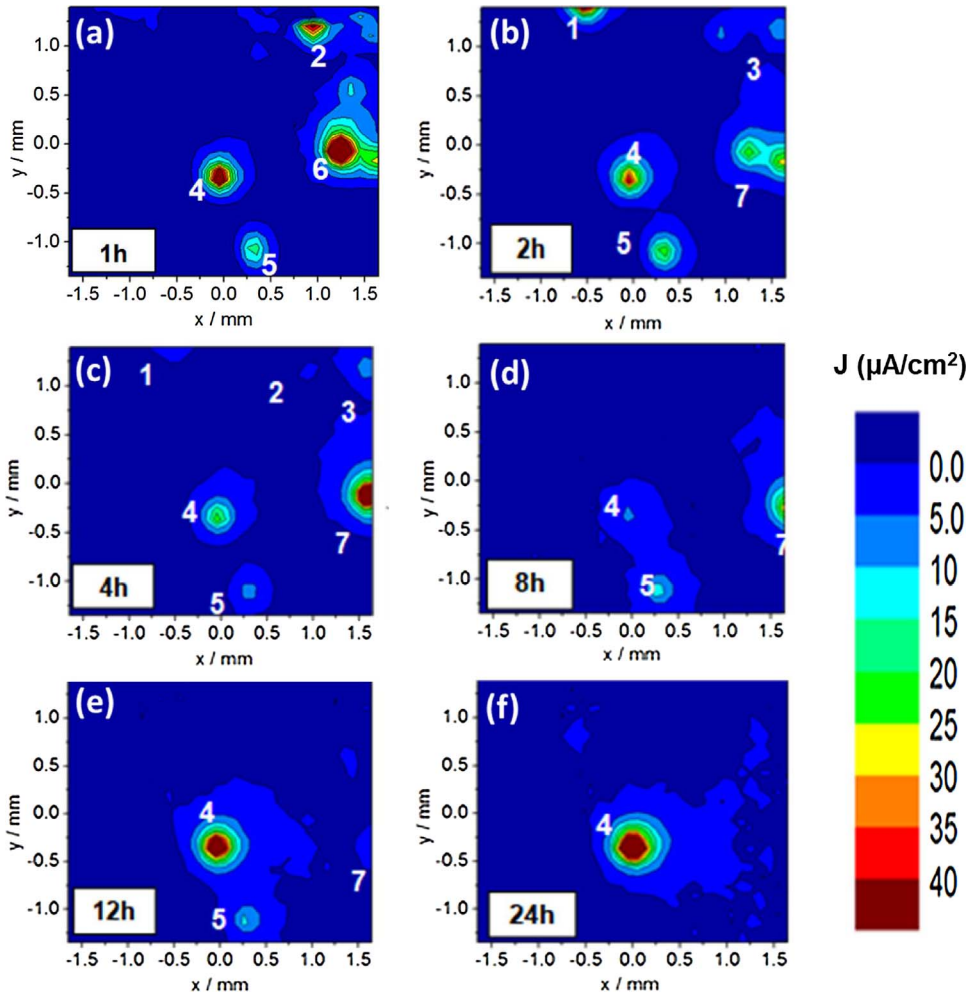

Fig. 8. SVET maps of AA2198-T851 after various times of immersion in 0.05 mol L^{-1} NaCl solution.

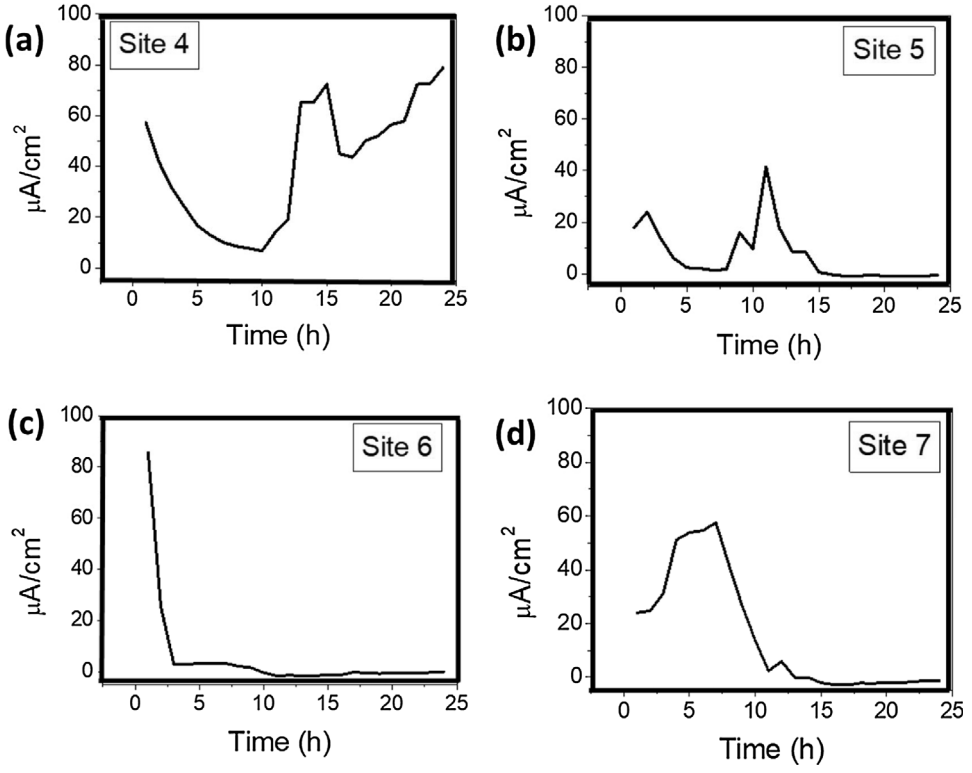

Fig. 9. Plots of peak current density values as a function of time of immersion in 0.05 mol L^{-1} NaCl solution at sites 4, 5, 6 and 7 as indicated in Fig. 8.

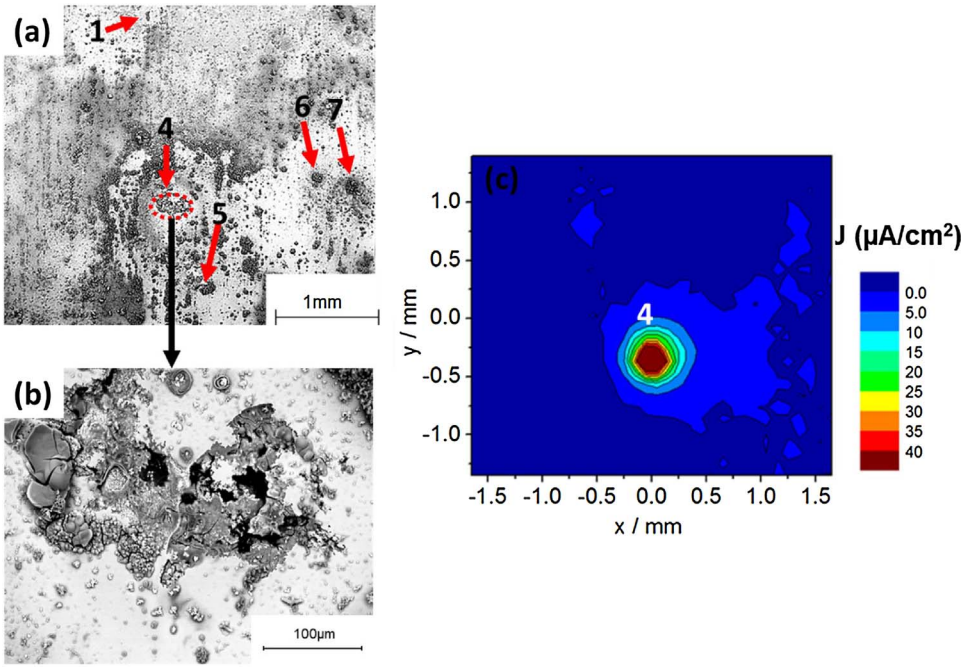

Fig. 10. (a) SEM micrograph of the surface of the AA2198-T851 alloy prior to removal of corrosion products. (b) Higher magnification micrograph of the circled region (corresponding to site 4 in the SVET maps) showing partially covered pit. (c) Corresponding SVET map of the surface of the alloy after 24 h of exposure to 0.05 mol L^{-1} NaCl solution.

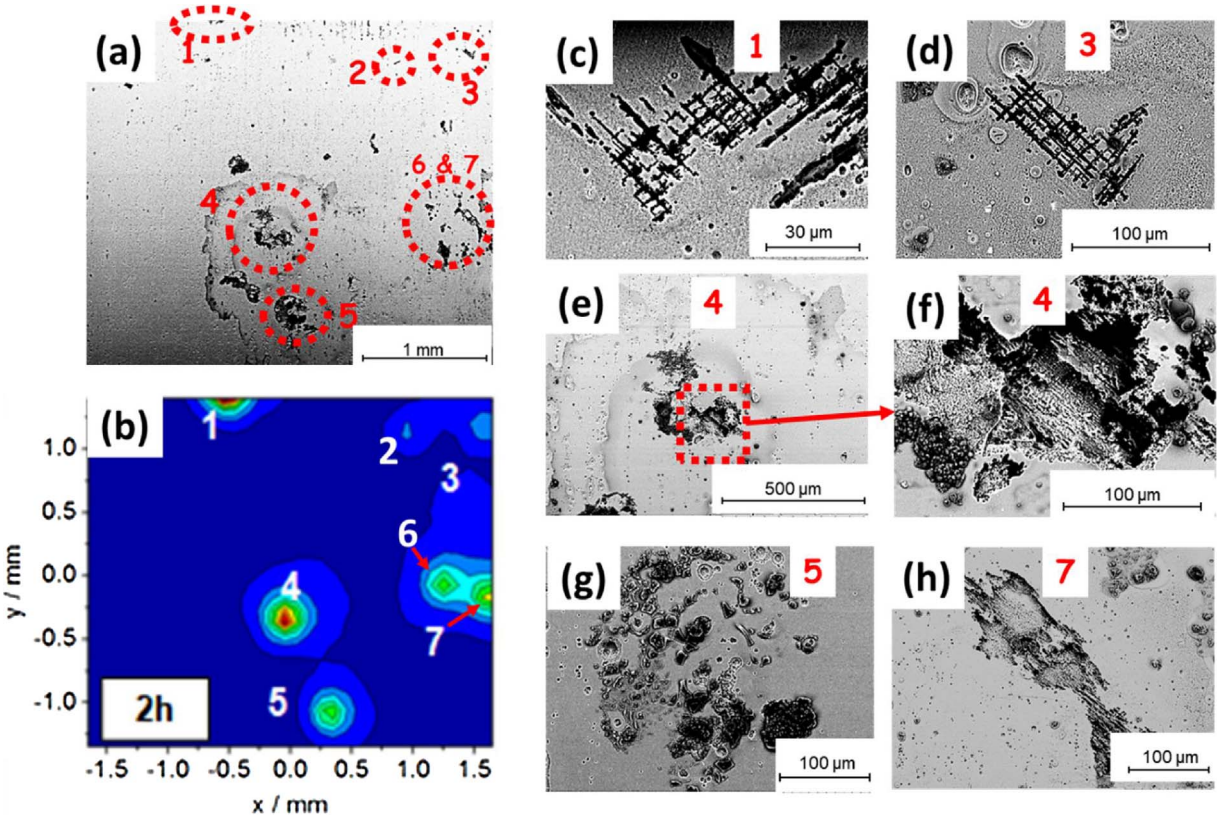

Fig. 11. (a) SEM micrograph of the surface of the AA2198-T851 alloy after the removal of corrosion products showing all the severe localized corrosion sites in agreement with the SVET map. (b) Corresponding SVET map of the surface of the alloy, after 2 h of exposure to 0.05 mol L^{-1} NaCl solution, showing current density peaks at the sites designated 1–7. (c)–(h) Magnified SEM micrographs of the zones labeled 1, 3, 4, 5 and 7 in (a).

slip bands in the grains of the alloys. The dislocation-rich zones in the slip bands favored preferential precipitation of the active T1 phase and, consequently, these zones were more susceptible to corrosion. Given that the propagation pathways are more aligned in $\{111\}_{Al}$, the orientations of the grains with respect to the exposed surface plays a major role in the crystallographic attack observed. In addition, high current density peaks were observed during SVET test from the early hours of exposure to the electrolyte which indicated that the AA2198-T851 is highly electrochemically active. Further, SVET results revealed that there was continuous deposition and detachment of corrosion products at the mouths of the pits (especially at the early hours of corrosion test), and that some sites were only partially covered with

corrosion products. Corrosion activities were more intense at the partially covered or uncovered pits and the current density values increased continuously at later hours of exposure. On the other hand, for the covered pits, corrosion activities diminished at later hours of exposure. Thus, with the aid of SVET, it was revealed that corrosion products play a key role in the overall extent of corrosion in the AA2198-T851 alloy.

Acknowledgments

The authors are grateful to FAPESP (Proc. 2013/13235-6) for financial support for this research, CAPES (Capes/Cofecub N°806-14) for the grants of M. X. Milagre, FAPESP (2017/03095-3) for the grants of U. Donatus and to LNANO for the provision of FEG/SEM and TEM analysis.

References

[1] T.H. Sanders Jr., E.A. Starke Jr., Aluminum-Lithium Alloys Proceedings of the 1st International Aluminum-Lithium Alloys, Metallurgical Society of AIME, 1981, pp. 63–68.
[2] T.H. Sanders Jr., E.A. Starke Jr., Aluminum-lithium alloys, Proceedings of the 2nd International Conference on Aluminum-Lithium Alloys (1983) 17–29.
[3] R. Rioja, J. Liu, The evolution of Al-Li base products for aerospace and space applications, Metall. Mater. Trans. 43 (2012) 3325–3337.
[4] M. Romios, R. Tiraschi, C. Parrish, H.W. Babel, J.R. Ogren, O.S. Es-Said, Design of multistep aging treatmentsof 2099 (C458) Al-Li alloy, Mater. Eng. Perform. 14 (2005) 641–646.
[5] R. Ambat, E.S. Dwarakadasa, The influence of pH on the corrosion of medium strength aerospace alloy-8090 alloy-2091 and alloy-2014, Corros. Sci. 33 (1992) 681–690.
[6] W.N. Garrard, Corrosion behavior of aluminum-lithium alloys, Corros. Sci. 50 (1994) 215–225.
[7] A.M. Semenov, Effect of Mg additions and thermal treatment on corrosion properties of Al-Li-Cu-base alloys, Prot. Met. 37 (2001) 126–131.
[8] T. Warner, Recently-developed aluminium solutions for aerospace applications, Mater. Sci. Forum. 519 (2006) 1271–1278.
[9] B. Noble, G.E. Thompson, T 1 (Al2CuLi) precipitation in aluminum–copper–lithium alloys, Metal Sci. J. 6 (1972) 167–174.
[10] M. Guérin, J. Alexis, E. Andrieu, L. Laffont, W. Lefebvre, G. Odemer, C. Blanc, Identification of the metallurgical parameters explaining the corrosion susceptibility in a 2050 aluminium alloy, Corros. Sci. 102 (2016) 291–300.
[11] V. Proton, J. Alexis, E. Andrieu, J. Delfosse, A. Deschamps, F. De Geuser, M.C. Lafont, C. Blanc, The influence of artificial ageing on the corrosion behaviour of a 2050 aluminium-copper-lithium alloy, Corros. Sci. 80 (2014) 494–502.
[12] V. Proton, J. Alexis, E. Andrieu, J. Delfosse, M.C. Lafont, C. Blanc, Characterisation and understanding of the corrosion behavior of the nugget in a 2050 aluminium alloy friction stir welding joint, Corros. Sci. 73 (2013) 130–142.
[13] R.G. Buchheit, D. Mathur, P.I. Gouma, Corrosion and Corrosion Prevention of Low Density Metals and Alloys, The Electrochemical Society, Pennington, New Jersey, 2001, pp. 444–452.
[14] J.E. Kertz, P.I. Gouma, R.G. Buchheit, Localized corrosion susceptibility of Al-Li-Cu-Mg-Zn alloy AF/C458 due to interrupted quenching from solutionizing, Metall. Mater. Trans. A 32 (2001) 2561–2573.
[15] W. Huang, Y. Ma, X. Zhou, X. Meng, Y. Liao, L. Chai, Y. Yi, X. Zhang, Correlation between localized plastic deformation and localised corrosion in AA2099 aluminum-lithium alloy, Surf. Interface Anal. 48 (2016) 745–749.
[16] Y. Ma, X. Zhou, W. Huang, Y. Liao, X. Chen, X. Zhang, Crystallographic defects induced localized corrosion in AA2099-T8 aluminium alloy, Corros. Eng. Sci. Technol. 50 (2015) 420–424.
[17] Y. Ma, X. Zhou, W. Huang, Y. Liao, X. Chen, X. Zhang, Localized corrosion in AA2099-T83 aluminum-lithium alloy: the role of grain orientation, Corros. Sci. 107 (2016) 41–48.
[18] Y. Ma, X. Zhou, Y. Liao, Y. Yi, H. Wu, Z. Wang, W. Huang, Localized corrosion in AA2099-T83 aluminium-lithium: the role of intermetallic particles, Mater. Chem. Phys. 161 (2014) 201–210.
[19] Y. Ma, X. Zhou, G.E. Thompson, M. Griffiths, R. Roberts, P. Thomson, M. Fowles, Distribution of intermetallics in an AA 2099-T8 aluminium alloy extrusion, Mater. Chem. Phys. 126 (2011) 46–53.
[20] R.C. Furneaux, G.E. Thompson, G.C. Wood, The application of ultramicrotomy to the electronoptical examination of surface films on aluminium, Corros. Sci. 18 (1978) 853–877.
[21] T. Hashimoto, X. Zhou, C. Luo, K. Kawano, G.E. Thompson, A.E. Hughes, P. Skeldon, P.J. Withers, T.J. Marrow, A.H. Sherry, Nantomography for understanding materials degradation, Scr. Mater. 63 (2010) 835–838.
[22] N. Birbilis, R.G. Buchheit, Electrochemical characteristics of intermetallic phases in aluminum alloys an experimental survey and discussion, J. Electrochem. Soc. 152 (2005) B140–B151.
[23] C. Luo, X. Zhou, T. Hashimoto, A. Hughes, G.E. Thompson, Study of localized corrosion in AA2024 aluminium alloy using electron tomography, Corros. Sci. 58 (2012) 299–306.
[24] J.F. Li, Z.Q. Zheng, N. Jiang, S.C. Li, Study on localized corrosion mechanism of 2195 Al-Li alloy in 4.0% NaCl solution (pH 6.5) using a three-electrode coupling system, Mater. Corr. 56 (2005) 192–196.
[25] K.L. Moore, J.M. Sykes, S.C. Hogg, P.S. Grant, Pitting corrosion of spray formed Al–Li–Mg alloys, Corr. Sci. 50 (2008) 3221–3226.
[26] J.A. Moreto, C.E.B. Marino, W.W. Bose Filho, L.A. Rocha, J.C.S. Fernandes, SVET, SKP and EIS study of the corrosion behaviour of high strength Al and Al–Li alloys used in aircraft fabrication, Corr. Sci. 84 (2014) 30–41.
[27] N.D. Alexopoulos, A. Proiou, W. Dietzel, C. Blawert, V. Heitmann, M. Zheludkevich, S.K. Kourkoulis, Mechanical properties degradation of (Al-Cu-Li) 2198 alloy due to corrosion exposure, Procedia Struct. Integr. 2 (2016) 597–603.
[28] J.A. Moreto, O. Gambonf, C.O.F.T. Rucherf, F. Romagnoli, M.F. Moreira, F. Beneduce, W.W. Bose Filho, Corrosion and fatigue behavior of new Al alloys, Procedia Eng. 10 (2011) 1521–1526.
[29] A.F.S. Santos, S. Zacarelli, S.R. de Araujo, F.M. Queiroz, M. Terada, I. Costa, Effect of Microstructure on the Corrosion Resistance of AA2524-T3 and AA2198-T851 Aluminum Alloys Used in the Aeronautic Industry, Eurocorr, Pisa, 2014.
[30] U. Donatus, M. Terada, C.R. Ospina, F.M. Queiroz, A.F.S. Bugarin, I. Costa, On the AA2198-T851 alloy microstructure and its correlation with localized corrosion behavior, Corros. Sci. 131 (2018) 300–309.
[31] J.C. Grosskreut, The mechanisms of metal fatigue (I), Phys. Stat. Sol. (b) 47 (1971) 11–31.
[32] K.S. Al-Rubaie, M.A. Del Grande, D.N. Travessa, K.R. Cardoso, Effect of pre-strain on the fatigue life of 7050-T7451 aluminium alloy, Mater. Sci. Eng. A 464 (2007) 141–150.
[33] H. Hao, D. Ye, Y. Chen, F. Mi, J. Liu, A study on the mean stress relaxation behavior of 2124-T851 aluminum alloy during low-cycle fatigue at different strain ratios, Mater. Des. 67 (2015) 272–279.
[34] M. Meiningers, L. Dicker Son, J.C. Gibe Ling, Observations of tension/compression asymmetry in the cyclic deformation of aluminum alloy 7075, Fatigue Fract. Eng. Mater. Struct. 19 (1996) 85–97.
[35] B.M. Gable, A.W. Zhu, A.A. Csontros, E.A. Starke, The role of plastic deformation on the competitive microstructural evolution and mechanical properties of a novel Al–Li–Cu–X alloy, J. Light Met. (2001) 1–14.
[36] B.M. Gable, A.A. Csontros, E.A. Starke, A quench sensitivity study on the novel Al–Li–Cu–X alloy AF/C 458J, Light Met. 2 (2002) 65–75.
[37] A.A. Csontros, E.A. Starke, The effect of inhomogeneous plastic deformation on the ductility and fracture behavior of age hardenable aluminum alloys, Int. J. Plast. 21 (2005) 1097–1118.
[38] M.A. Muñoz-Morris, I. Gutierrez-Urrutia, N. Calderon, D.G. Morris, Refinement of precipitates and deformation substructure in an Al–Cu–Li alloy during heavy rolling at elevated temperature, Mater. Sci. Eng. A 492 (2008) 268–275.
[39] R.G. Bucheit, J.P. Moran, G.E. Stoner, Electrochemical behavior of the T1 (Al_2CuLi) intermetallic compound and its role in localized corrosion of Al-2% Li-3% Cu alloys, Corrosion 50 (1994) 120–130.
[40] X. Zhang, X. Zhou, T. Hashimoto, B. Liu, C. Luo, Z. Sun, Z. Tang, F. Lu, Y. Ma, Corrosion behaviour of 2A97-T6 Al-Cu-Li alloy: the influence of non-uniform precipitation, Corros. Sci. (2017) (in press).
[41] W. Zhang, G.S. Frankel, Anisotropy of localized corrosion in AA2024-T3, Electrochem. Solid-State Lett. 3 (2000) 268–270.
[42] W. Zhang, G.S. Frankel, Transitions between pitting and intergranular corrosion in AA2024, Electrochim. Acta 48 (2003) 1193–1210.
[43] M. Guérin, J. Alexis, E. Andrieu, L. Laffonta, W. Lefebvre, G. Odemera, C. Blanc, Identification of the metallurgical parameters explaining the corrosion susceptibility in a 2050 aluminium alloy, Corros. Sci. 102 (2016) 291–300.
[44] J.F. Li, Z.Q. Zheng, N. Jiang, S.C. Li, Study on localized corrosion mechanism of 2195 Al-Li alloy in 4.0% NaCl solution (pH 6.5) using a three-electrode coupling system, Mater. Corros. 56 (2005) 192–196.
[45] J.F. Li, C.X. Li, Z.W. Peng, W.J. Chen, Z.Q. Zheng, Corrosion mechanism associated with T1 and T2 precipitates of Al–Cu–Li alloys in NaCl solution, J. Alloys Compd. 460 (2008) 688–693.